LETTER

Topological energy transfer in an optomechanical system with exceptional points

H. Xu[1], D. Mason[1], Luyao Jiang[1] & J. G. E. Harris[1,2]

Topological operations can achieve certain goals without requiring accurate control over local operational details; for example, they have been used to control geometric phases and have been proposed as a way of controlling the state of certain systems within their degenerate subspaces[1–8]. More recently, it was predicted that topological operations can be used to transfer energy between normal modes, provided that the system possesses a specific type of degeneracy known as an exceptional point[9–11]. Here we demonstrate the transfer of energy between two vibrational modes of a cryogenic optomechanical device using topological operations. We show that this transfer arises from the presence of an exceptional point in the spectrum of the device. We also show that this transfer is non-reciprocal[12–14]. These results open up new directions in system control; they also open up the possibility of exploring other dynamical effects related to exceptional points[15,16], including the behaviour of thermal and quantum fluctuations in their vicinity.

An externally imposed time variation of the Hamiltonian H of an otherwise isolated, conservative system provides a powerful means for controlling the evolution of the system. If H is varied sufficiently slowly, then the adiabatic theorem states that a system prepared at some initial time t_0 in a non-degenerate normal mode of $H(t_0)$ will remain in the corresponding normal mode of the instantaneous $H(t)$ (ref. 17). As a result, varying H so as to execute a closed loop (in the space of parameters that define H) will return the system to its initial state, up to an overall phase. This phase was shown by Berry and others to include a contribution that is determined by a simple geometric property of the control loop[1–4]. The subsequent insight that such a topological operation (that is, executing a closed control path) may have an outcome that is robust against small fluctuations in the control path has had a profound impact on many areas of theory and experiment[5–8,18].

More recently, it was predicted[9–11] that topological operations may also be used to transfer energy between modes in systems that are subject to loss and/or gain. Specifically, energy transfer was predicted to occur for closed adiabatic control paths that enclose an exceptional point (EP, a form of degeneracy that can arise when the effective Hamiltonian is non-Hermitian; also known as a branch point). It was also predicted[12–14] that such operations can be non-reciprocal in their dependence on the initial conditions of the system and the direction of rotation of the control loop about the EP. The possibility of using topological operations to control the energy distribution within a system while also inducing non-reciprocal behaviour has attracted considerable attention[19–22]. Some features of EPs have been demonstrated in static measurements of spectra and eigenmodes[23,24]; however, experiments have not yet realized topological or non-reciprocal dynamics by encircling an EP.

Here we measure topological and non-reciprocal dynamics in an optomechanical system. We show that the system possesses an EP and that external control parameters can be used to encircle the EP on timescales comparable to the lifetime of the excitations of the system. We demonstrate that such topological operations can transfer energy and that this energy transfer is non-reciprocal. When the control path

is not adiabatic, the dynamics becomes more complicated; however, we find quantitative agreement between experimental data and numerical simulations over the full range of measurements.

The system studied here consists of a silicon nitride membrane placed inside a high-finesse optical cavity[25]. The dimensions of the membrane are $1\,\text{mm} \times 1\,\text{mm} \times 50\,\text{nm}$. Because it is almost perfectly square, the vibrational eigenmodes of the membrane include nearly degenerate pairs that are well-separated in frequency from all the other eigenmodes. We use this separation to focus on a nearly degenerate pair with natural frequencies $\omega_1/(2\pi) = 788.024\,\text{kHz}$ and $\omega_2/(2\pi) = 788.487\,\text{kHz}$. In the absence of laser light driving the optical cavity, these two modes are essentially uncoupled and have very small damping rates ($\gamma_1/(2\pi) = 0.6\,\text{Hz}$ and $\gamma_2/(2\pi) = 1.4\,\text{Hz}$).

When a laser excites the cavity, the resultant intracavity field α drives the vibrations of the membrane via radiation pressure. At the same time, these vibrations detune the cavity and thereby modulate α (refs 25, 26). It is straightforward to integrate $\alpha(t)$ out of the full optomechanical equations of motion (see Methods), resulting in an effective equation of motion for just c_1 and c_2, the displacements of the modes of the membrane:

$$i\dot{\boldsymbol{C}}(t) = H\boldsymbol{C}(t) \qquad (1)$$

where $\boldsymbol{C}(t) = [c_1(t), c_2(t)]^{\text{T}}$. The effective Hamiltonian is

$$H = \begin{pmatrix} \omega_1 - i\dfrac{\gamma_1}{2} - ig_1^2\sigma & -ig_1g_2\sigma \\[2mm] -ig_1g_2\sigma & \omega_2 - i\dfrac{\gamma_2}{2} - ig_2^2\sigma \end{pmatrix} \qquad (2)$$

where $g_{1,2}$ are the optomechanical coupling rates of the mechanical modes, and the complex mechanical susceptibility introduced by the intracavity field is

$$\sigma = \frac{P}{\hbar\Omega_{\text{L}}} \frac{\kappa_{\text{in}}}{(\kappa/2)^2 + \Delta^2} \left[\frac{1}{\kappa/2 - i(\omega_0 + \Delta)} - \frac{1}{\kappa/2 + i(-\omega_0 + \Delta)} \right] \qquad (3)$$

Here P and Ω_{L} are the power and frequency of the laser driving the cavity, Δ is the mean detuning between the laser and the cavity, $\omega_0 = (\omega_1 + \omega_2)/2$, and κ and κ_{in} are the linewidth and input coupling rate of the cavity, respectively. The experiment described here is classical; the reduced Planck constant $\hbar$ appears in the expression for σ because $g_{1,2}$ are given in terms of the single-photon rate.

The system will possess an EP if σ can be made to equal $(\omega_1 - i\gamma_1/2 - \omega_2 + i\gamma_2/2)\left[-i(g_1^2 - g_2^2) \pm 2g_1g_2\right]/(g_1^2 + g_2^2)^2$. Achieving this typically requires control over both $\text{Re}(\sigma)$ and $\text{Im}(\sigma)$. For optomechanical devices in the resolved sideband regime ($\kappa < \omega_0$), this control is provided by P and Δ. By contrast, when $\kappa \gg \omega_0$, P and Δ appear in σ in a linearly dependent fashion and so control only $|\sigma|$. The ability to access (and encircle) an EP using the detuning and power of a single laser is an important feature of the system presented here (and

[1]Department of Physics, Yale University, New Haven, Connecticut 06511, USA. [2]Department of Applied Physics, Yale University, New Haven, Connecticut 06511, USA.
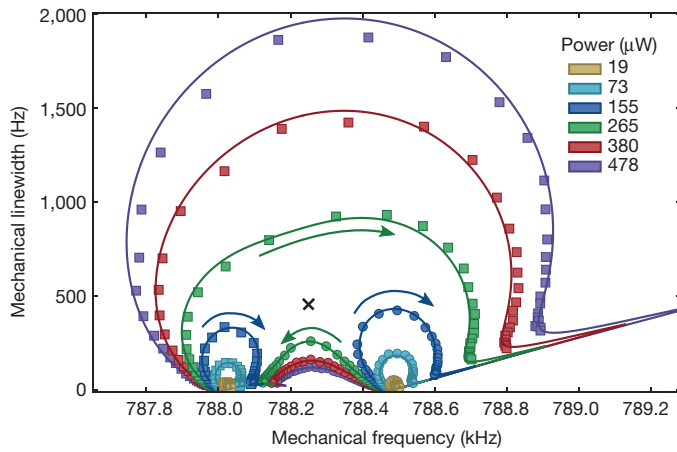
Figure 1 | The complex eigenvalues of the normal modes of the membrane. The resonance frequency (horizontal axis) and damping rate (vertical axis) of the two mechanical modes of the membrane as a function of the laser power P and detuning Δ. Data for one mode are shown as squares; data for the other mode are shown as circles. The statistical uncertainty in the measurements is smaller than the symbols. Colours indicate P, while the arrows indicate the variation of the eigenvalues as Δ is varied from $-1,200$ kHz to -400 kHz at fixed P. For the lower values of P, each eigenvalue follows a closed trajectory, beginning and ending at the same point. For the higher values of P, the eigenvalues follow open trajectories, each one ending at the starting point of the other. The solid lines are the global fit described in the text. The location of the EP predicted by this fit is shown as a black cross.

in contrast with the more complicated arrangement proposed in ref. 27), because these parameters can be controlled *in situ* with a high degree of precision, timing accuracy, and dynamic range.

A detailed description of the optomechanical device and the measurement set-up is given in Methods. The membrane and optical cavity are maintained at $T = 4.2$ K. The motion of the membrane is monitored via a heterodyne measurement of a laser with constant power and detuning. Control over the optomechanical system is

provided by a separate laser, whose detuning Δ and power P are set by an acousto-optic modulator.

To establish the presence of an EP in this system, we measured the mechanical spectrum of the membrane as a function of Δ and P. These spectra were acquired by driving the membrane and monitoring its response via the heterodyne signal. As described in Methods, each spectrum was fitted to determine the two resonance frequencies $\omega_{a,b}(\Delta, P)$ and damping rates $\gamma_{a,b}(\Delta, P)$. (The subscripts 'a' and 'b' refer to the normal modes of the membrane in the presence of an optical field; the subscripts '1' and '2' used previously refer to these modes in the absence of an optical field.)

The results of these fits are summarized in Fig. 1, which shows the complex eigenvalues $\xi_{a,b} = \omega_{a,b} - i\gamma_{a,b}/2$ as Δ and P are varied. When $P \lesssim 155\,\mu$W, ξ_a and ξ_b each trace out a closed trajectory, completing a loop as Δ is varied from $\ll -\omega_0$ to $\gg -\omega_0$. By contrast, when $P \gtrsim 265\,\mu$W, ξ_a and ξ_b both follow open trajectories, swapping their values as Δ is varied over the same range. This sharp transition in the topology of $\xi_{a,b}(\Delta)$ is characteristic of an EP[9]. The solid lines in Fig. 1 are a global fit to the complex eigenvalues of H, which gives best-fit values of $\omega_{1,2}$ and $\gamma_{1,2}$ as stated above, as well as $g_1/(2\pi) = 1.03$ Hz, $g_2/(2\pi) = 1.14$ Hz, $\kappa_{in}/(2\pi) = 70$ kHz and $\kappa/(2\pi) = 177$ kHz. These values imply the existence of an EP at $\Delta_{EP}/(2\pi) = -792.5$ kHz, $P_{EP} = 223\,\mu$W (or equivalently $\omega_{EP}/(2\pi) = 788.2$ kHz and $\gamma_{EP}/(2\pi) = 460$ Hz, indicated as the black cross in Fig. 1).

Figure 2a, b shows measurements of $\mathrm{Re}(\xi_{a,b})$ and $-2\mathrm{Im}(\xi_{a,b})$ over a narrow range of Δ and P centred on Δ_{EP} and P_{EP}. These measurements show the characteristic features of an EP: ξ_a and ξ_b coalesce at a single value of the control parameters and, in the vicinity of this point, they exhibit the same structure as the Riemann sheets of the complex square-root function $z^{1/2}$. For comparison, Fig. 2c, d shows the eigenvalues of H (see equation (2)), calculated using the best-fit values determined in Fig. 1.

The surfaces shown in Fig. 2a, b are such that if Δ and P were varied to execute a single closed loop, the resulting smooth evolution on the eigenvalue manifold would return to its starting point only if the loop did not enclose the EP. By contrast, a loop enclosing the EP would result in a trajectory starting on one sheet, but ending on the other.
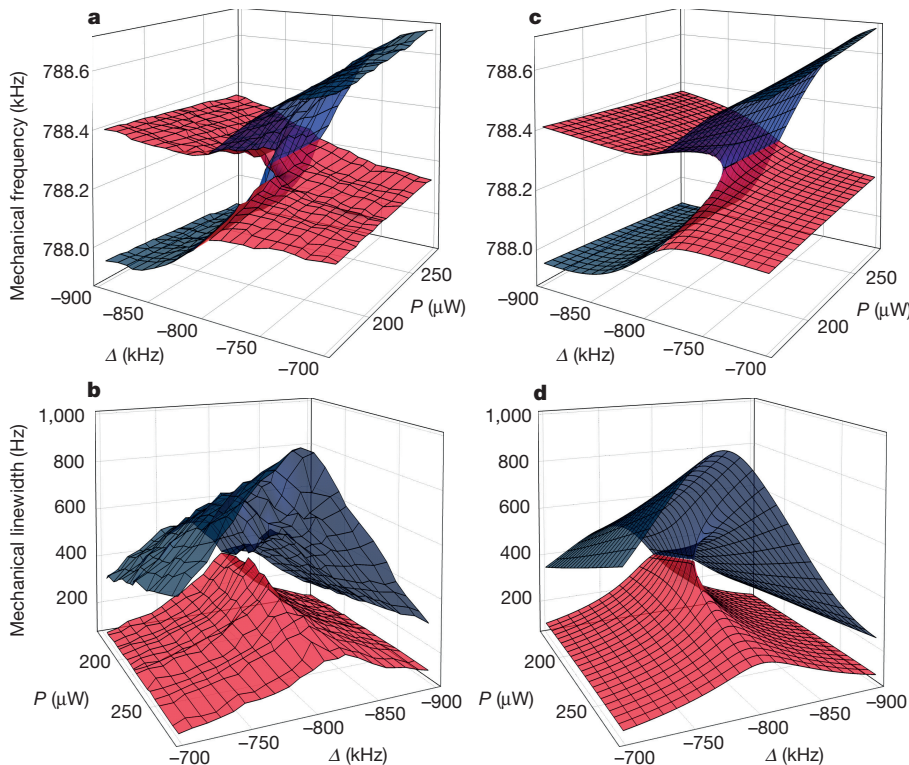
Figure 2 | The exceptional point in the spectrum of mechanical modes. a, b, The resonance frequencies (**a**) and damping rates (**b**) of the two mechanical modes of the membrane as a function of laser power P and detuning Δ. Each grid point corresponds to a measurement; grid lines and surface colouring are guides to the eye. Colouring is chosen so that red (blue) corresponds to the mode with lower (higher) damping. **c, d,** Plots of the theoretically calculated real (**c**) and imaginary (**d**) parts of the eigenvalues of the effective Hamiltonian matrix H (equation (2)). All of the parameters appearing in this calculation are taken from the fit in Fig. 1. Note that the viewing angle in **a** and **c** differs from that in **b** and **d**.
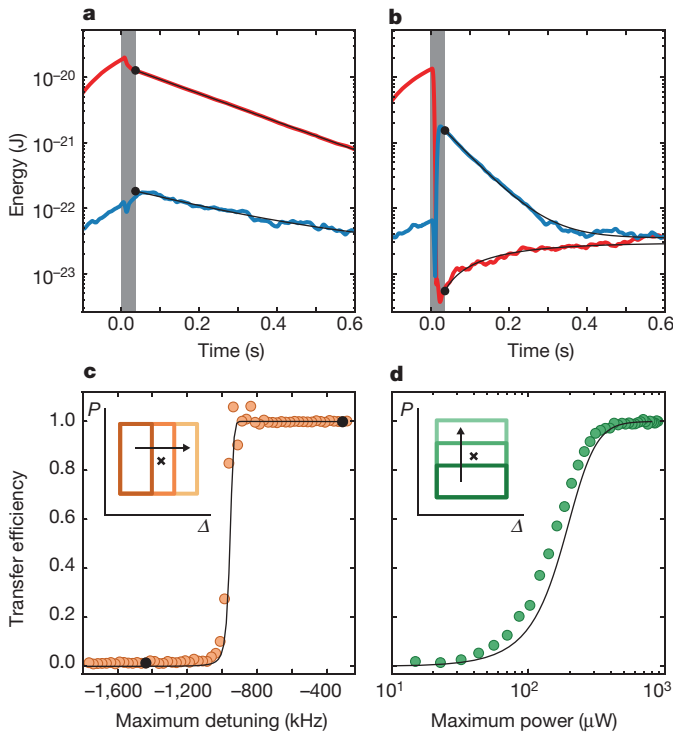
Figure 3 | Topological energy transfer. a, b, The energies of mode 'a' (red) and mode 'b' (blue) as a function of time t. A drive is applied to the 'a' mode for $t < 0$. At $t = 0$ the drive is turned off and the control loop described in the text is implemented. The control loop ends at $t = 16$ ms; the grey shaded region corresponds to the time during which the control loop is implemented. For $t > 16$ ms the system relaxes to thermal equilibrium. The black lines are fits to a decaying exponential (due to the mechanical damping) with a constant offset (reflecting the thermal motion of the mode). The black dot shows the extrapolation of this fit to $t = 16$ ms. The loop used in **a** does not enclose the EP, whereas the loop used in **b** does. **c,** The fraction of the (remaining) energy in the 'b' mode after the control loop has been completed as a function of the maximum detuning of the loop, Δ_{max}. The left (right) point shown as a solid circle corresponds to the data in **a** (**b**). **d,** The corresponding measurement as a function of the maximum power of the loop, P_{max}. In **c** and **d**, the statistical errors are comparable to or smaller than the size of the symbols. The solid lines are numerical simulations of the dynamics and are completely constrained by the parameters from the fit in Fig. 1. The insets are schematics showing how the loop varies along the horizontal axis of each panel; the location of the EP is indicated by the black cross.

To observe this effect, we performed a series of measurements in which Δ and P were initially set to Δ_{max} and P_{min}, and one of the modes of the membrane (c_a) was excited using a piezoelectric element. Once the system reached its steady state, the piezo drive was switched off, and Δ and P were varied to sweep out a closed rectangular loop. The loop was defined by the points (Δ_{max}, P_{min}), (Δ_{max}, P_{max}), (Δ_{min}, P_{max}) and (Δ_{min}, P_{min}), returning to (Δ_{max}, P_{min}) after a duration $\tau = 16$ ms. This value of τ was chosen so that nearly all such control loops satisfy the requirement of conventional adiabaticity: $\tau \gg 1/|\xi_a - \xi_b|$ (loops passing close to the EP do not satisfy this inequality). We describe the effect of varying τ below.

The heterodyne signal was recorded before, during and after the control loop. This signal was demodulated at frequencies $\omega_a(\Delta_{max}, P_{min})$ and $\omega_b(\Delta_{max}, P_{min})$, with typical results shown in Fig. 3a, b. Before and after the control loop (that is, for $t < 0$ and $t > \tau$), this record corresponds to the amplitudes of the motion of the normal modes $|c_a(t)|$ (red in Fig. 3a, b) and $|c_b(t)|$ (blue). During the control loop ($0 \le t \le \tau$) this correspondence does not hold, because the eigenfrequencies of the membrane undergo rapid variations; data from this region do not play any role in our analysis. As shown in Fig. 3a, b, c_a is initially excited to about 4×10^{-12} m. There is also a small excitation of c_b

(owing to the non-zero overlap of the mechanical resonances); however, this unintentional excitation accounts for less than about 1% of the total energy, and does not qualitatively affect the results presented here.

Comparing $|c_{a,b}(0)|$ with $|c_{a,b}(\tau)|$ in Fig. 3a, b, it is clear that energy is lost from the system during the control loop. This reflects the fact that the damping here is always positive. To distinguish this overall energy loss from effects related to the topological operation, we focus on the relative energy of the two modes before and after the loop.

The data in Fig. 3a were taken for a control loop that did not enclose the EP ($\Delta_{max} = -1,440$ kHz, $P_{max} = 750$ μW; for all data, $\Delta_{min} = -1,890$ kHz, $P_{min} = 2$ μW). As a result, the nearly adiabatic transit around the control loop results in negligible energy transfer at the end of the control loop. This can be seen qualitatively in Fig. 3a by noting that approximately 99% of the energy is in c_a both immediately before and immediately after the control loop.

By contrast, Fig. 3b shows a measurement in which the control loop does enclose the EP ($\Delta_{max} = -300$ kHz, $P_{max} = 750$ μW). The effect on the dynamics is readily visible: before the loop more than 99% of the energy is in c_a, whereas after the loop more than 99% of the (remaining) energy is in c_b.

To quantify the transfer of energy from one mode to another, we define the efficiency $E = |c_b(\tau)|^2/[|c_a(\tau)|^2 + |c_b(\tau)|^2]$ (this definition makes use of the fact that, before the loop, nearly all the energy is in c_a). The values of $|c_{a,b}(\tau)|$ are determined by fitting decaying exponentials to $|c_{a,b}(t)|$ for $t > \tau + 20$ ms and extrapolating these fits to $t = \tau$.

Figure 3c shows $E(\Delta_{max})$ for fixed $P_{max} = 750$ μW; Fig. 3d shows $E(P_{max})$ for fixed $\Delta_{max} = -290$ kHz. The limiting behaviour in both cases (that is, for large or small P_{max} and Δ_{max}) agrees with the prediction that adiabatic paths enclosing the EP will result in energy transfer, whereas adiabatic paths not enclosing the EP will not. The solid lines in Fig. 3c, d are the results of numerically integrating equations (1) and (2), and are not fits; rather, they use the $P(t)$ and $\Delta(t)$ used in the measurements, and the values of $g_{1,2}$, $\omega_{1,2}$, $\gamma_{1,2}$, κ_{in} and κ determined from the data in Fig. 1. These simulations show good agreement with the measurements irrespective of whether the loop encloses the EP and of whether the loop satisfies adiabaticity.

The measurements shown in Fig. 3 were all made by applying the initial drive to the 'a' mode and then executing a control loop in the counter-clockwise sense. In this case, the adiabatic trajectories enclosing the EP correspond to the less-damped eigenmode (red regions of the surfaces in Fig. 2) for the majority of the loop. By contrast, executing the same loop in the clockwise sense would result in an adiabatic trajectory corresponding primarily to the more-damped eigenmode (blue regions in Fig. 2). As described in refs 12–14, 28, adiabatic behaviour is expected while the system is in the less-damped eigenmode; however, when the system is in the more-damped mode, competition between the non-adiabatic transfer (which is exponentially small in τ) and the effect of differential loss (which is exponentially large in τ) leads to a breakdown of adiabaticity, causing the system to eventually relax to the less-damped mode. This process may also be understood as a consequence of the Stokes phenomenon of asymptotics[12].

This behaviour is demonstrated in Fig. 4, which shows $E(\tau)$ when the EP is encircled in the counter-clockwise or clockwise sense, and with the initial excitation in the 'a' mode (for which E is as defined above) or the 'b' mode (for which E is as defined above, but with the subscripts reversed). The same loop was used in all four cases: $\Delta_{min} = -1,890$ kHz, $P_{min} = 2$ μW, $\Delta_{max} = -290$ kHz and $P_{max} = 750$ μW. In all four cases, executing the loop very quickly results in negligible energy transfer ($E \to 0$ as $\tau \to 0$), consistent with the conventional expectation for a sudden perturbation.

The adiabatic limit ($\tau \gg 1$ ms) is quite different. Efficient energy transfer is achieved ($E \to 1$) for an initial excitation in the 'a' mode and a counter-clockwise loop (and for an initial excitation in the 'b' mode and a clockwise loop), consistent with the discussion of Fig. 3, and with the fact that these conditions correspond to adiabatic paths almost entirely in the less-damped mode. By contrast, $E \to 0$ when $\tau \gg 1$ ms
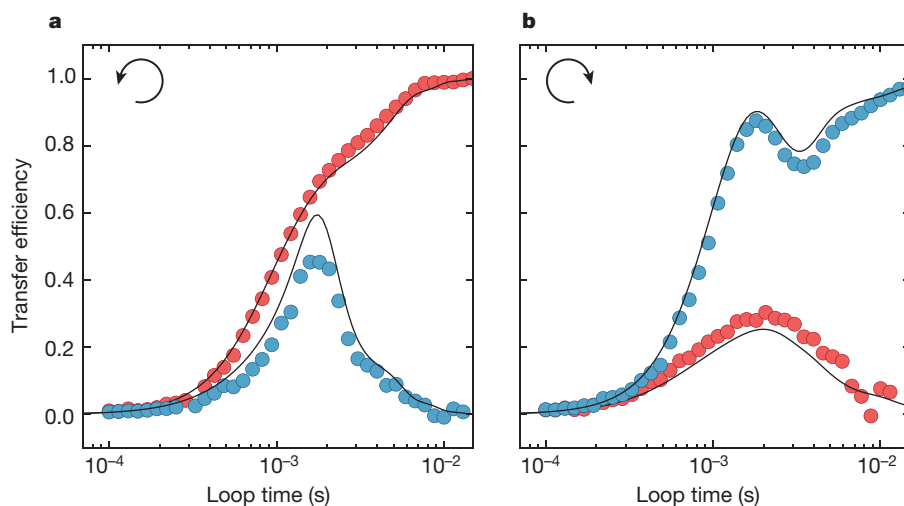
Figure 4 | Non-reciprocal topological dynamics.
a, **b**, The transfer efficiency E as a function of the duration of the control loop, τ. The loop shape is identical for all four data series and encloses the EP. The loop is counter-clockwise in **a** and clockwise in **b**, as indicated by the arrows. Red (blue) circles represent data for which the 'a' ('b') mode is initially driven. In all four cases, rapid encircling around the EP ($\tau \rightarrow 0$) results in vanishing energy transfer ($E \rightarrow 0$). For adiabatic encircling, the limiting behaviour of E depends on the sense of the loop and which mode is initially excited. For counter-clockwise (clockwise) loops, the red (blue) data correspond to conventional adiabaticity ($E \rightarrow 1$ as τ increases) and the blue (red) data show the opposite behaviour ($E \rightarrow 0$ as τ increases). As described in the text, this reflects the non-reciprocity of each topological operation (counter-clockwise or clockwise loop). The solid lines are numerical simulations of the dynamics and are completely constrained by the parameters from the fit in Fig. 1.

for an initial excitation in the 'b' mode and a counter-clockwise loop (and for an initial excitation in the 'a' mode and a clockwise loop).

The behaviour described above may be summarized by describing an adiabatic control loop around an EP as a matrix that transforms the initial state $\boldsymbol{C}(0) = [c_1(0), c_2(0)]^T$ to the final state $\boldsymbol{C}(\tau) = [c_1(\tau), c_2(\tau)]^T$ with the form:

$$U_{\circlearrowleft,\circlearrowright}(\tau) = \begin{pmatrix} a_{\circlearrowleft,\circlearrowright}(\tau) & b_{\circlearrowleft,\circlearrowright}(\tau) \\ c_{\circlearrowleft,\circlearrowright}(\tau) & d_{\circlearrowleft,\circlearrowright}(\tau) \end{pmatrix} \qquad (4)$$

where $\circlearrowleft$ and $\circlearrowright$ denote a counter-clockwise and clockwise loop, respectively. Because H is a symmetric matrix, it is straightforward to show that if $U_{\circlearrowleft}(\tau)$ and $U_{\circlearrowright}(\tau)$ represent identical but time-reversed control loops, then $U_{\circlearrowleft} = U_{\circlearrowright}^T$. Along with this relationship, the four data-sets in Fig. 4 demonstrate the non-reciprocity of these operations, that is, that $b_{\circlearrowleft,\circlearrowright}(\tau) \neq c_{\circlearrowleft,\circlearrowright}(\tau)$ for $\tau \gg 1$ ms (ref. 29). This inequality is also evident in direct measurements of $|b_{\circlearrowleft,\circlearrowright}(\tau)|$ and $|c_{\circlearrowleft,\circlearrowright}(\tau)|$ (see Methods).

We have demonstrated a new form of adiabatic topological operation that allows for non-reciprocal energy transfer between two eigenmodes of a mechanical system. This transfer exploits the presence of an EP in the spectrum of the two modes. The square membrane used here also offers threefold and fourfold near-degeneracies, opening up the possibility of studying dynamics in the vicinity of higher-order EPs[15,16]. Furthermore, the cryogenic optomechanical device used here is subject to both thermal and quantum fluctuations[30]; it is an open question whether non-reciprocal topological effects will allow for new forms of control over these fluctuations.

1. Simon, B. Holonomy, the quantum adiabatic theorem, and Berry's phase. *Phys. Rev. Lett.* **51**, 2167–2170 (1983).
2. Berry, M. V. Quantal phase factors accompanying adiabatic changes. *Proc. R. Soc. Lond. A* **392**, 45–57 (1984).
3. Berry, M. V. Classical adiabatic angles and quantal adiabatic phase. *J. Phys. A* **18**, 15–27 (1985).
4. Hannay, J. H. Angle variable holonomy in adiabatic excursion of an integrable Hamiltonian. *J. Phys. A* **18**, 221–230 (1985).
5. Arovas, D., Schrieffer, J. R. & Wilczek, F. Fractional statistics and the quantum Hall effect. *Phys. Rev. Lett.* **53**, 722–723 (1984).
6. Tomita, A. & Chiao, R. Y. Observation of Berry's topological phase by use of an optical fiber. *Phys. Rev. Lett.* **57**, 937–940 (1986).
7. Kitaev, A. Y. Fault-tolerant quantum computation by anyons. *Ann. Phys.* **303**, 2–30 (2003).
8. Nayak, C., Simon, S. H., Stern, A., Freedman, M. & Das Sarma, S. Non-Abelian anyons and topological quantum computation. *Rev. Mod. Phys.* **80**, 1083–1159 (2008).
9. Heiss, W. D. Phases of wave functions and level repulsion. *Euro. Phys. J. D* **7**, 1–4 (1999).
10. Keck, F., Korsch, H. J. & Mossmann, S. Unfolding a diabolic point: a generalized crossing scenario. *J. Phys. A* **36**, 2125–2137 (2003).
11. Berry, M. V. Physics of nonhermitian degeneracies. *Czech. J. Phys.* **54**, 1039–1047 (2004).
12. Berry, M. V. & Uzdin, R. Slow non-Hermitian cycling: exact solutions and the Stokes phenomenon. *J. Phys. A* **44**, 435303 (2011).
13. Uzdin, R., Mailybaev, A. & Moiseyev, N. On the observability and asymmetry of adiabatic state flips generated by exceptional points. *J. Phys. A* **44**, 435302 (2011).
14. Milburn, T. J. *et al.* General description of quasiadiabatic dynamical phenomena near exceptional points. *Phys. Rev. A* **92**, 052124 (2015).
15. Cartarius, H., Main, J. & Wunner, G. Exceptional points in the spectra of atoms in external fields. *Phys. Rev. A* **79**, 053408 (2009).
16. Demange, G. & Graefe, E.-M. Signatures of three coalescing eigenfunctions. *J. Phys. A* **45**, 025303 (2012).
17. Arnold, V. I. *Mathematical Methods of Classical Mechanics* Ch. 10 (Springer, 1989).
18. Ando, T., Nakanishi, T. & Saito, R. Berry's phase and absence of back scattering in carbon nanotubes. *J. Phys. Soc. Jpn* **67**, 2857–2862 (1998).
19. Lefebvre, R., Atabek, O., Šindelka, M. & Moiseyev, N. Resonance coalescence in molecular photodissociation. *Phys. Rev. Lett.* **103**, 123003 (2009).
20. Hamamda, M., Pillet, P., Lignier, H. & Comparat, D. Ro-vibrational cooling of molecules and prospects. *J. Phys. B* **48**, 182001 (2015).
21. Kaprálová-Žďánská, P. R. & Moiseyev, N. Helium in chirped laser fields as a time-asymmetric atomic switch. *J. Chem. Phys.* **141**, 014307 (2014).
22. Kim, S. Braid operation of exceptional points. *Fortschr. Phys.* **61**, 155–161 (2013).
23. Philipp, M., von Brentano, P., Pascovici, G. & Richter, A. Frequency and width crossing of two interacting resonances in a microwave cavity. *Phys. Rev. E* **62**, 1922–1926 (2000).
24. Dembowski, C. *et al.* Experimental observation of the topological structure of exceptional points. *Phys. Rev. Lett.* **86**, 787–790 (2001).
25. Thompson, J. D. *et al.* Strong dispersive coupling of a high-finesse cavity to a micromechanical membrane. *Nature* **452**, 72–75 (2008).
26. Aspelmeyer, M., Kippenberg, T. J. & Marquardt, F. Cavity optomechanics. *Rev. Mod. Phys.* **86**, 1391–1452 (2014).
27. Jing, H. *et al.* $\mathcal{PT}$-symmetric phonon laser. *Phys. Rev. Lett.* **113**, 053604 (2014).
28. Graefe, E.-M., Mailybaev, A. A. & Moiseyev, N. Breakdown of adiabatic transfer of light in waveguides in the presence of absorption. *Phys. Rev. A* **88**, 033842 (2013).
29. Jalas, D. *et al.* What is — and what is not — an optical isolator. *Nat. Photon.* **7**, 579–582 (2013).
30. Underwood, M. *et al.* Measurement of the motional sidebands of a nanogram-scale oscillator in the quantum regime. *Phys. Rev. A* **92**, 061801 (2015).

Author Contributions H.X., D.M. and L.J. performed the measurements and analysed the data. J.G.E.H. and H.X. wrote the manuscript with input from all the authors. J.G.E.H. directed the research.

Author Information Reprints and permissions information is available at www.nature.com/reprints. The authors declare no competing financial interests. Readers are welcome to comment on the online version of the paper. Correspondence and requests for materials should be addressed to J.G.E.H. (jack.harris@yale.edu).

METHODS

Measurement set-up. A schematic illustration of the experiment is shown in Extended Data Fig. 1. The optomechanical device and much of the measurement set-up are described in ref. 30. The membrane and optical cavity are mounted in a cryostat that is maintained at $T = 4.2\,\text{K}$. The motion of the membrane is monitored via a heterodyne measurement using a probe beam and a local oscillator, both produced from a single laser ('ML' in Extended Data Fig. 1a). The probe-beam frequency is shifted by an acousto-optical modulator (AOM1 in Extended Data Fig. 1a) driven at 80 MHz. Pound–Drever–Hall locking is used to keep the probe beam nearly resonant with one mode of the cavity; as a result its detuning $\Delta_\text{p} \ll \kappa$, resulting in a negligible contribution to σ. Likewise, the large detuning of the local oscillator ($\Delta_\text{LO} \approx 80\,\text{MHz} \gg \kappa$) also results in a negligible contribution to σ. Control over the optomechanical system is provided by a separate laser ('CL' in Extended Data Fig. 1a), whose detuning Δ and power P are controlled by an additional acousto-optic modulator (AOM3 in Extended Data Fig. 1a). The frequencies of the various beams are illustrated in Extended Data Fig. 1b. The cavity is approximately single-sided and all measurements are performed in reflection. The reflected beams are incident on a single photodiode, and demodulation circuits are used to monitor multiple Fourier components of the heterodyne signal, each with a bandwidth equal to 50 Hz.

Optically mediated mechanical coupling. We consider a system consisting of two mechanical modes, each coupled linearly to a common optical mode. We show that the optical field generates a tunable effective coupling between the mechanical modes, which can be exploited to produce an EP, as described in the main text. The model closely follows the one presented in ref. 31.

In a standard optomechanical system, one considers an optical cavity mode with a frequency that is linearly coupled to the position of a mechanical oscillator. An input–output approach to this system yields a pair of coupled differential equations for the two modes, which can be easily treated in the Fourier domain to understand the optical modification of the mechanical susceptibility. Here we consider a simple extension of this model in which there are two mechanical modes, each coupled to the same optical mode. This yields the following equations of motion for the mechanical/optical modes:

$$\dot{a} = -\left(\frac{\kappa}{2} + i\omega_\text{c}\right)a - ig_1 az_1 - ig_2 az_2 + \sqrt{\kappa_\text{in}}\,a_\text{in}$$

$$\dot{c}_1 = -\left(\frac{\gamma_1}{2} + i\omega_1\right)c_1 - ig_1 a^* a + \sqrt{\gamma_1}\,\eta_1$$

$$\dot{c}_2 = -\left(\frac{\gamma_2}{2} + i\omega_2\right)c_2 - ig_2 a^* a + \sqrt{\gamma_2}\,\eta_2$$

where a is the optical mode amplitude with resonant frequency ω_c, total dissipation rate κ and input coupling rate κ_in. The ith mechanical mode is described by position $z_i = c_i + c_i^*$, where c_i is the complex mode amplitude and the asterisks indicate complex conjugation. Each mechanical mode has resonant frequency ω_i, dissipation rate γ_i, and is coupled to the optical mode with a single-photon coupling rate g_i. The optical and mechanical modes are driven by input fields a_in and η_i, respectively.

We now suppose that the cavity is driven by a beam with power P and frequency Ω_L, detuned from the cavity resonance by $\Delta = \Omega_\text{L} - \omega_\text{c}$. By doing so, we can express the optical field as fluctuations $d(t)$ around a mean intracavity field given by

$$\bar{a} = \frac{\sqrt{\kappa_\text{in}}}{\frac{\kappa}{2} - i\Delta}\,a_\text{in}; \quad a_\text{in} = \sqrt{\frac{P}{\hbar\Omega_\text{L}}}$$

Making these substitutions in the original system of equations yields the linearized equations of motion:

$$\dot{d} = -\left(\frac{\kappa}{2} - i\Delta\right)d - i\alpha_1 z_1 - i\alpha_2 z_2$$

$$\dot{c}_1 = -\left(\frac{\gamma_1}{2} + i\omega_1\right)c_1 - i(\alpha_1^* d + \alpha_1 d^*) + \sqrt{\gamma_1}\,\eta_1$$

$$\dot{c}_2 = -\left(\frac{\gamma_2}{2} + i\omega_2\right)c_2 - i(\alpha_2^* d + \alpha_2 d^*) + \sqrt{\gamma_2}\,\eta_2$$

where we have defined $\alpha_i = \bar{a}g_i$. Moving to the Fourier domain, and defining the cavity susceptibility $\chi_\text{c}(\omega) = [\kappa/2 - i(\omega + \Delta)]^{-1}$, we solve for $d(\omega)$ and $d^*(\omega)$ and substitute these into the equations for $c_{1,2}(\omega)$ to find a reduced system of two equations describing the mechanical modes:

$$\left[\frac{\gamma_1}{2} - i(\omega - \omega_1)\right]c_1(\omega) = |\alpha_1|^2 \left[\chi_\text{c}^*(-\omega) - \chi_\text{c}(\omega)\right]c_1(\omega)$$
$$+ \alpha_1^*\alpha_2\left[\chi_\text{c}^*(-\omega) - \chi_\text{c}(\omega)\right]c_2(\omega)$$

$$\left[\frac{\gamma_2}{2} - i(\omega - \omega_2)\right]c_2(\omega) = |\alpha_2|^2 \left[\chi_\text{c}^*(-\omega) - \chi_\text{c}(\omega)\right]c_2(\omega)$$
$$+ \alpha_1^*\alpha_2\left[\chi_\text{c}^*(-\omega) - \chi_\text{c}(\omega)\right]c_1(\omega)$$

Note that we have dropped counter-rotating c_1^* and c_2^* terms. We have also dropped the mechanical drive terms $\eta_{1,2}$. These are not necessary for our model, because we drive the system to a particular initial state, turn off the drive and then focus on the evolution of the system without any mechanical drive applied.

In the traditional optomechanical system, one defines the (single-mode) optomechanical self-energy as $\Sigma_\text{SM}(\omega) = i\,|\alpha|^2\,[\chi_\text{c}^*(-\omega) - \chi_\text{c}(\omega)]$. In this two-mode system, we can extend this concept to a self-energy matrix:

$$\Sigma = \begin{pmatrix} i|\alpha_1\alpha_1| & i|\alpha_1\alpha_2| \\ i|\alpha_2\alpha_1| & i|\alpha_2\alpha_2| \end{pmatrix} [\chi_\text{c}^*(-\omega) - \chi_\text{c}(\omega)] = \begin{pmatrix} -ig_1^2\sigma & -ig_1g_2\sigma \\ -ig_1g_2\sigma & -ig_2^2\sigma \end{pmatrix} \quad (5)$$

where σ is defined in equation (3).

Writing our mechanical modes as a vector $\boldsymbol{C}(t) = [c_1(t), c_2(t)]^\text{T}$, we can write the following matrix equation:

$$-i\omega\boldsymbol{C}(\omega) = -\begin{pmatrix} \frac{\gamma_1}{2} + i\omega_1 & 0 \\ 0 & \frac{\gamma_2}{2} + i\omega_2 \end{pmatrix}\boldsymbol{C}(\omega) - i\Sigma(\omega)\boldsymbol{C}(\omega)$$

Before we move back to the time domain, we note that $\Sigma(\omega)$ varies on the scale of κ, whereas the mechanical modes are susceptible to drives only within their linewidth, which is substantially smaller than κ, by assumption. Therefore, it is sufficient to consider $\Sigma(\omega) \approx \Sigma(\omega_1) \approx \Sigma(\omega_2) \equiv \Sigma$. (The mechanical modes are also assumed to be nearly degenerate.) Now that Σ is not a function of ω, we can easily move back to the time domain to obtain equation (1) (reprinted here for convenience):

$$i\dot{\boldsymbol{C}}(t) = H\boldsymbol{C}(t)$$

where we define

$$H = \begin{pmatrix} \omega_1 - i\frac{\gamma_1}{2} & 0 \\ 0 & \omega_2 - i\frac{\gamma_2}{2} \end{pmatrix} + \Sigma \quad (6)$$

Here Σ is a complex quantity, which depends (via α_1 and α_2) on P and Δ. This is the tunability that allows us to access an EP in the spectrum of the two mechanical modes.

We note that equation (6) is identical to equation (2); the apparent difference is due to the fact that in equation (2) the matrix Σ is expressed using the right-most form in equation (5).

Measuring the mechanical eigenvalue spectrum. In Figs 1 and 2, we show the presence of an EP in the complex eigenvalue spectrum (frequencies and decay rates) of the mechanical modes. At each point (P, Δ), the eigenvalues were measured by optically driving the mechanical modes and measuring their driven response. We measure the mechanical sidebands using the heterodyne measurement laser, locked to the cavity resonance. We set a certain P and Δ for the control laser, then apply amplitude modulation at a frequency near ω_1 and ω_2, thus creating an optical beat note that drives the mechanical modes. This modulation frequency is swept over ω_1 and ω_2, and we use a lock-in amplifier to measure the complex response of the heterodyne signal to this drive.

Two examples of these measurements are shown here. Extended Data Fig. 2 shows a sweep over the two modes when the control-beam power is low and there is minimal hybridization of the two modes. In Extended Data Fig. 3, the control-beam power is large and detuned near $-\omega_{1,2}$ such that the modes hybridize substantially, resulting in modes with nearly degenerate frequencies, but different linewidths. The relative phase of the driven response of the two modes is such that we see destructive interference in Extended Data Fig. 3. By fitting the complex response to a sum of complex Lorentzians with an arbitrary phase offset, we extract ω_1, ω_2, γ_1 and γ_2. The solid lines in Extended Data Figs 2 and 3 are these fits, from which we extract the eigenvalues plotted in Figs 1 and 2.

EPs have also been observed in many other systems, including atom–cavity composites[32], microwave cavities[23,24], optical systems[33–36], electronic circuits[37] and an exciton–polariton system[38], and are predicted to exist in Bose–Einstein condensates[39,40], quantum dots[41], acoustic systems[42], magnetohydrodynamic dynamos[43] and nuclei[44].

Measurement of propagator matrix elements. Figure 4 shows the non-reciprocity of the topological operations as parameterized by their energy transfer efficiency E. The non-reciprocity of these operations can also be seen from direct measurements of the magnitudes of the matrix elements defined in equation (4). These measurements are carried out by, for example, initially driving the 'a' mode and then performing a clockwise loop about the EP; in this case $|a_\circlearrowleft(\tau)| = |c_a(\tau)/c_a(0)|$ and $|c_\circlearrowleft(\tau)| = |c_b(\tau)/c_a(0)|$. Similarly, repeating this process, but with the 'b' mode initially driven, gives $|b_\circlearrowleft(\tau)|$ and $|d_\circlearrowleft(\tau)|$. In Extended Data Fig. 4, we plot the magnitudes of these propagator matrix elements as a function of the loop duration τ. The points in Extended Data Fig. 4 are extracted from the same data as shown in Fig. 4. For sufficiently large τ, we see that $|b_{\circlearrowright,\circlearrowleft}(\tau)| \neq |c_{\circlearrowright,\circlearrowleft}(\tau)|$, as stated in the main text, which implies $U_{\circlearrowright,\circlearrowleft}(\tau) \neq U_{\circlearrowright,\circlearrowleft}^{\mathrm{T}}(\tau)$.

The real-time dynamics studied here can be connected to the propagation of light through an optical crystal with properties that vary along the beam path[12,45]. An encircling around an EP is also mapped onto the propagation through a two-mode waveguide in a concurrent experiment[46].

31. Shkarin, A. B. et al. Optically mediated hybridization between two mechanical modes. Phys. Rev. Lett. **112,** 013602 (2014).
32. Choi, Y. et al. Quasieigenstate coalescence in an atom-cavity quantum composite. Phys. Rev. Lett. **104,** 153601 (2010).
33. Lee, S.-B. et al. Observation of an exceptional point in a chaotic optical microcavity. Phys. Rev. Lett. **103,** 134101 (2009).
34. Brandstetter, M. et al. Reversing the pump dependence of a laser at an exceptional point. Nat. Commun. **5,** 4034 (2014).
35. Peng, B. et al. Loss-induced suppression and revival of lasing. Science **346,** 328–332 (2014).
36. Zhen, B. et al. Spawning rings of exceptional points out of Dirac cones. Nature **525,** 354–358 (2015).
37. Stehmann, T., Heiss, W. D. & Scholtz, F. G. Observation of exceptional points in electronic circuits. J. Phys. A **37,** 7813–7819 (2004).
38. Gao, T. et al. Observation of non-Hermitian degeneracies in a chaotic exciton-polariton billiard. Nature **526,** 554–558 (2015).
39. Heiss, W. D. & Nazmitdinov, R. G. Instabilities, nonhermiticity and exceptional points in the cranking model. J. Phys. A **40,** 9475–9481 (2007).
40. Cartarius, H., Main, J. & Wunner, G. Discovery of exceptional points in the Bose-Einstein condensation of gases with attractive $1/r$ interaction. Phys. Rev. A **77,** 013618 (2008).
41. Weidenmüller, H. A. Crossing of two Coulomb blockade resonances. Phys. Rev. B **68,** 125326 (2003).
42. Wu, T.-T. & Huang, Z.-G. Level repulsions of bulk acoustic waves in composite materials. Phys. Rev. B **70,** 214304 (2004).
43. Günther, U., Stefani, F. & Gerbeth, G. The MHD α^2-dynamo, Z_2-graded pseudo-Hermiticity, level crossings and exceptional points of branching type. Czech. J. Phys. **54,** 1075–1089 (2004).
44. Michel, N., Nazarewicz, W., Okołowicz, J. & Płoszajczak, M. Open problems in the theory of nuclear open quantum systems. J. Phys. G **37,** 064042 (2010).
45. Berry, M. V. Optical polarization evolution near a non-Hermitian degeneracy. J. Opt. **13,** 115701 (2011).
46. Doppler, J. et al. Dynamically encircling an exceptional point for asymmetric mode switching. Nature http://www.dx.doi.org/10.1038/nature18605 (2016).
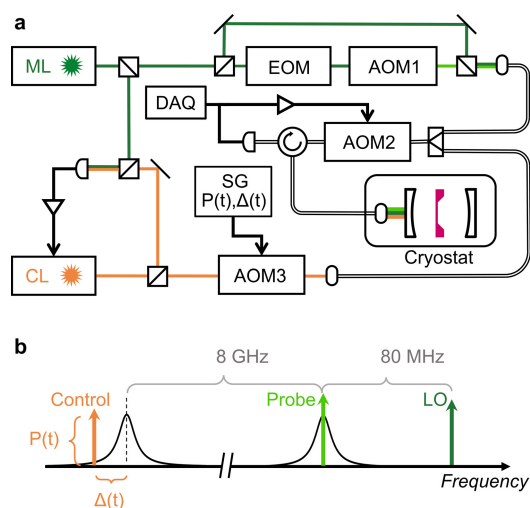
Extended Data Figure 1 | Experimental schematics. a, Illustration of the optical and electronic components. The measurement laser ('ML') is split into a local oscillator ('LO' in **b**) and a probe beam ('Probe' in **b**). The probe-beam frequency is shifted by an acousto-optic modulator ('AOM1'), and is locked to the cavity using a Pound–Drever–Hall (PDH) scheme and modulation produced by an electro-optic modulator ('EOM'). The control laser ('CL'; 'Control' in **b**) is locked to the measurement laser with a frequency offset that is approximately double the free spectral range of the cavity. The control parameters used to access the EP are the power P and detuning Δ of the control laser. P and Δ are set by the amplitude and frequency of a signal generator ('SG'), which drives another acousto-optic modulator ('AOM3'). The PDH error signal is used to control the frequency of yet another acousto-optic modulator ('AOM2'), ensuring that all beams track fluctuations of the cavity. Light is delivered to (and collected from) the cryostat via an optical circulator. Coloured lines, hollow lines and thick black lines show free-space laser beams, optical fibres and electrical circuits, respectively. Triangles, ovals and semicircles show electronics, fibre couplers and photodiodes, respectively. 'DAQ' indicates the data acquisition system. The silicon nitride membrane is shown in purple. **b**, Illustration of the optical frequency domain. Lasers are indicated by coloured arrows and cavity modes by black curves.
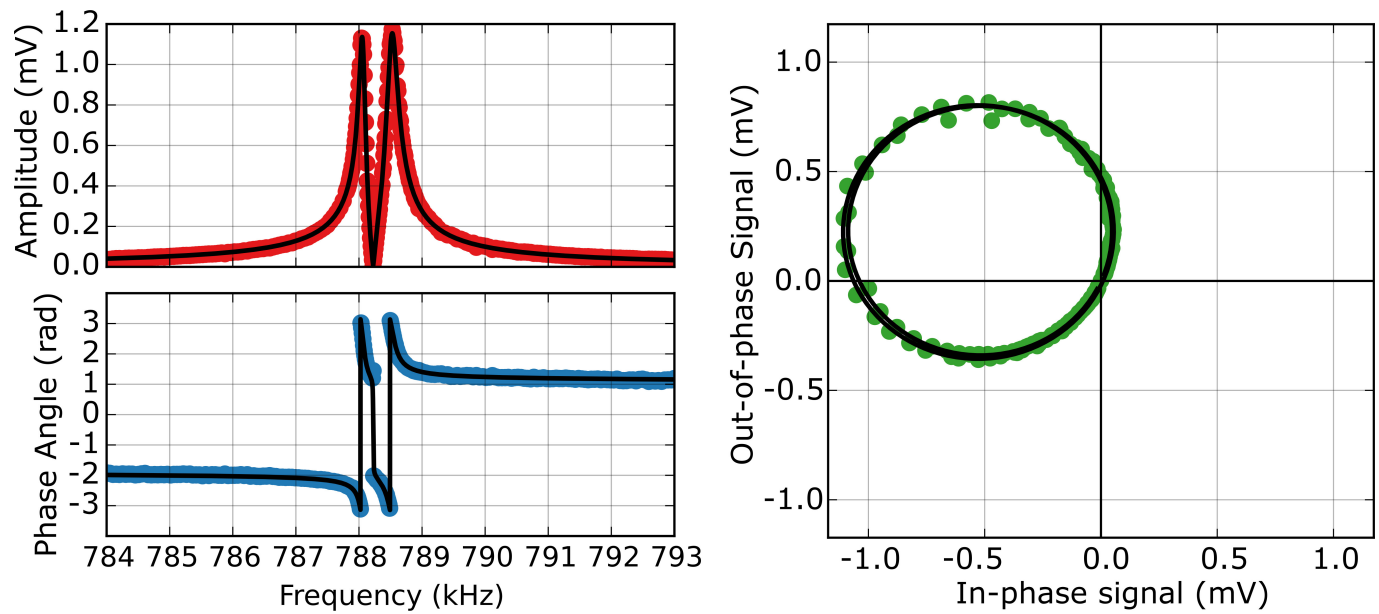
Extended Data Figure 2 | Lock-in signal at low laser power ($\Delta = -780\,\text{kHz}$, $P = 73\,\mu\text{W}$). Left, amplitude (top, red) and phase angle (bottom, blue) of the lock-in signal as a function of drive frequency. Right, the same data shown as a parametric plot of the in-phase and out-of-phase components of the lock-in signal as a function of drive frequency.
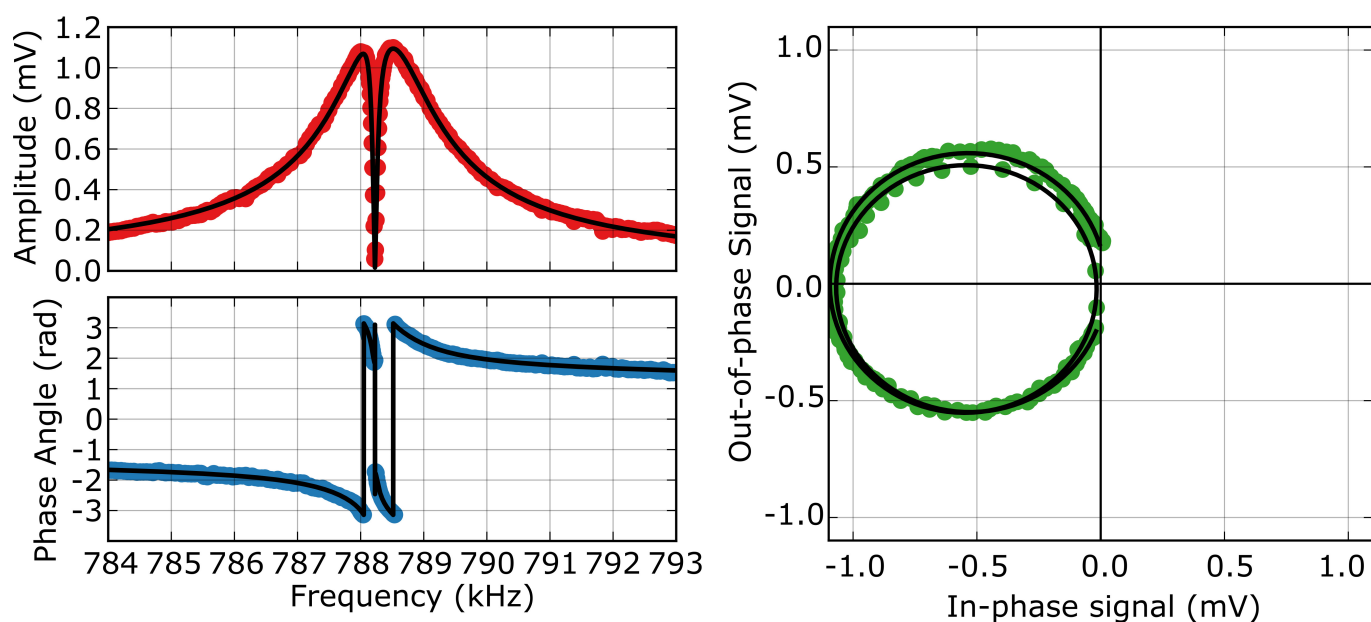
Extended Data Figure 3 | Lock-in signal at high laser power ($\Delta = -780\,\mathrm{kHz}$, $P = 380\,\mu\mathrm{W}$). Left, amplitude (top, red) and phase angle (bottom, blue) of the lock-in signal as a function of drive frequency. Right, the same data shown as a parametric plot of the in-phase and out-of-phase components of the lock-in signal as a function of drive frequency.
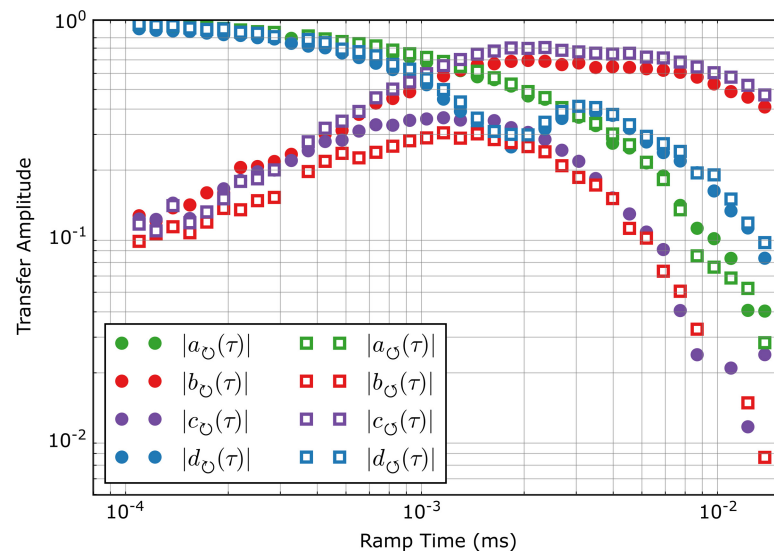
Extended Data Figure 4 | Magnitudes of propagator matrix elements.